Journal of Alloys and Compounds 1002 (2024) 175322

Contents lists available at ScienceDirect

Journal of Alloys and Compounds

journal homepage: www.elsevier.com/locate/jalcom

How to design plasmonic Ag/$SrTiO_3$ nanocomposites as efficient photocatalyst: Theoretical insight and experimental validation

Quang Thang Trinh [a,1,*], Tuyen Le Van [b,1], Thi To Nga Phan [b,1], Khuong Phuong Ong [c], Hendrik Kosslick [d], Prince Nana Amaniampong [e], Michael B. Sullivan [c], Hong-Son Chu [c], Hongjie An [a], Tuan-Khoa Nguyen [a], Jun Zhang [a], Jia Zhang [c,*], Pham Thanh Huyen [b,*], Nam-Trung Nguyen [a,*]

[a] Queensland Micro and Nanotechnology Centre, Griffith University, Nathan, Queensland 4111, Australia
[b] School of Chemistry and Life Sciences, Hanoi University of Science and Technology, Viet Nam
[c] Institute of High Performance Computing (IHPC), Agency for Science, Technology and Research (A*STAR), 1 Fusionopolis Way, #16-16 Connexis, Singapore 138632, Singapore
[d] Institute of Chemistry, Rostock University, Germany
[e] Institut de Chimie des Milieux et Matériaux de Poitiers, University of Poitiers, CNRS 1 rue Marcel Doré, Poitiers 86073, France

ARTICLE INFO

Keywords:
Computational modelling
Electronic metal-support interactions (EMSI)
Density Functional Theory (DFT) calculations
Plasmonic nanocomposites
Environmental remediation
Heterostructure Interface
Heterogeneous photocatalyst

ABSTRACT

An integrated theoretical-experimental investigation is performed to understand the photocatalytic and optical properties of Ag/$SrTiO_3$ nanocomposite (Ag/STO). Theoretical investigation reveals that the catalytic activity of Ag/STO is increased when Ag particle size is smaller, while the opposite correlation is observed for its visible-light absorbance efficiency. These insights suggest that efficient Ag/STO photocatalyst needs to be balanced between the active interfacial site density and visible-light absorbance intensity by carefully controlling the Ag dosage. Furthermore, reactive oxygen species that are responsible for the oxidative degradation of organic pollutant on Ag/STO could be identified from Density Functional Theory (DFT) calculations. Comprehensive experiments are carried out using Rhodamine-B (RhB) photodegradation to test the activity of Ag/STO in wastewater treatment application and excellently validate those theoretical predictions. Over series of synthesized Ag/STO composites with different Ag contents, the optimum 1 % wt. Ag loading has the highest 92.8 % efficiency in RhB photodegradation after 1 hour of light irradiation. Trapping experiments also confirm the crucial role of O_2 and OH species, which was predicted from DFT calculations, as the primary oxidizing agents for the degradation of RhB. This work provides a useful framework to develop novel plasmonic nanocomposites for other photocatalytic applications.

1. Introduction

The rapid industrialization growth and drastically global population booming makes clean water shortage a serious threat to the survival and development of humanity. It is predicted that approximately 4–5 billion people will be affected by the global water shortage and water-borne illness by 2050 [1]. One most important target of the UN Sustainable Development Goals (SDG) from 2015 to 2030 is to ensure the "clean, accessible water for all," which requires the development of novel materials science and innovative technologies that generate the fit-for-purpose water from other resources such as briny water, seawater and wastewater [2]. Therefore, the development of new technologies that are both pollution-free and able to utilize alternative clean energy resources for wastewater remediation is becoming an urgent task.

Among possible solutions that have been reported, photocatalysis has appeared as one of the most suitable approaches due to its ability to utilize solar energy which is the most renewable and abundant resource [3–5]. Recent advances in the design of novel photocatalysts, especially the rational construction of heterostructural photocatalysts, enable the photocatalytic reactions as highly efficient platforms to address the

* Corresponding authors.
E-mail addresses: q.trinh@griffith.edu.au (Q.T. Trinh), zhangj@ihpc.a-star.edu.sg (J. Zhang), huyen.phamthanh@hust.edu.vn (P.T. Huyen), nam-trung.nguyen@griffith.edu.au (N.-T. Nguyen).
[1] These authors contribute equally to this paper.

https://doi.org/10.1016/j.jallcom.2024.175322
Received 20 May 2024; Received in revised form 17 June 2024; Accepted 23 June 2024
Available online 24 June 2024

sustainable development and achieve the Zero net emission via water splitting [6], CO_2 utilization [7–10], hydrogen production [11–13], and nitrogen fixation [14] processes. In this context, several photocatalytic materials have been developed and tested for water decontamination [15–17]. However, these catalysts suffer from poor stability and low activity, hindering their large-scale deployments for practical applications. Hence, the need to develop a more robust, catalytically active, and stable photocatalyst is crucial.

Strontium titanate perovskite ($SrTiO_3$, denoted as STO) is a promising material with many advantages, including the abundance of constituent elements, high chemical stability, high photochemical stability, strong catalytic activity, and good biological compatibility. Those advantages make STO as one of the most suitable and practical photocatalyst for water treatment [18–20]. One of the biggest advantages of STO compared to the conventional solar absorbent TiO_2 is its appropriate conduction band position making the charge transfer to the electron acceptor more feasible, resulting to its higher photocatalytic efficiencies [21–23]. However, the photo absorption spectrum of STO is still limited to the Ultra-Violet (UV) range because of its wide 3.2 eV energy gap, hindering the efficiency of solar-energy conversion. Several methods to modify the STO material to enable it absorbing the solar visible light for photocatalytic applications have been performed by tuning its electronic structure, such as noble metal decorating [24], narrow bandgap semiconductor coupling [25], introduction of oxygen vacancy [26], and transition metal ion doping [27].

Among the above approaches, decorating perovskite with plasmonic nanostructures (such as Ag, Au and Pt nanoparticles) has attracted great attention due to the merit of the intense light absorption upon depositing those metals on the perovskite. It was reported that decorating the wide bandgap semiconductors with plasmonic nanostructures could extend the light absorption ability of the materials to the visible range and resulting in better photocatalytic activities [28]. The incoming photons can interact strongly with the surface electrons of those plasmonic nanostructures when their oscillating frequencies are overlapped, inducing to the so-called “localized surface plasmon resonance” (LSPR) [29]. This phenomenon is characteristic by a significant enhancement of light absorption at the desired wavelengths and depends on the type of metals and varies with different shapes and sizes of the metal nanoparticles [30–32].

Besides the ability in absorbing solar energy, efficient photocatalysts also need to possess a high density of active sites to generate reactive agents that are essential for photo-catalytic reactions. Supporting metal nanoparticles on the perovskite possess interfacial sites having the properties which are modified by the electronic metal-support interactions (EMSI) and could be very much different from the metals and the perovskite separately [33]. If appropriately designed, these interfacial sites could significantly enhance the reaction activity [34–37]. However, the typical scale to design and control the properties of the interfacial sites is the molecular scale - a scale which is arduous to access experimentally, especially for complicated structures of metal supported on perovskite. First principles-based molecular modelling on the other hand is most suitable to study the molecular-level effects and is helpful in guiding and validating the chemical intuition at the atomistic and molecular scale [38–42]. Zhang et al. performed density functional theory (DFT) investigation to reveal the detailed CO oxidation mechanism on TM/STO catalysts (TM = Ir, Ag, Rh, Pd, Au and Pt) and explained the unresolved structure-performance relationships obtained from experimental literature [43]. This work also predicted that doping STO with fluorine (F) could further enhance the catalytic CO oxidation of TM/STO catalysts beyond the current experimental findings. Qureshi et al. combined DFT calculations with experimental characterizations to study the photocatalytic water splitting on a $Pt/SrTiO_3$ catalyst and identified that the EMSI between STO and ultrafine Pt clusters (sizer smaller than 2 nm) was indeed the main reason resulting in the high activity [44]. Despite those efforts, understanding the photocatalytic activity of perovskite-based plasmonic nanocomposites remains in its infancy and their optical properties are usually not considered in those studies. Those limits currently hinder the computationally driven design of efficient perovskite-based materials in photocatalytic applications.

In this study, systematic computational approaches are used to reveal the insight into interfacial catalytic activities and optical properties of Ag/STO nanocomposites. Atomic-scale simulations are performed using DFT calculations to understand the electronic properties and interaction at the interface between Ag and STO phases. The combination of DFT simulations and numerical physical modelling is carried out to study the changes of optical properties with different sizes of Ag nanoparticles. Based on the knowledge gained from theoretical investigations, the strategy to design the Ag/STO catalysts that have optimum photocatalytic activity will be derived. Subsequently, theoretical predictions will be confirmed by experiments. The liquid phase deposition is used for fabrication of Ag/STO plasmonic nanocomposites with different loadings of Ag nanoparticles. The photocatalytic activity of $Ag/SrTiO_3$ nanocomposites in the degradation of Rhodamine B (RhB) was investigated over a series of Ag/STO composites with different amounts of Ag to evaluate their application in eliminating organic pollutants in water. Subsequently, the optimum catalyst will be comprehensively characterized, and its reusability will be examined to evaluate its real-world practicability.

2. Computational and experimental methods

2.1. Computational methods

2.1.1. Density functional theory (DFT) calculations

The Vienna ab-initio simulation program (VASP) [45,46] was used to performed all the spin-polarized DFT calculations in this study, using the projector-augmented wave (PAW) scheme and a plane-wave basis set with a 520 eV cut-off kinetic energy. A PBE+U Hubbard scheme with U = 4.36 eV for Ti atoms adopted from earlier studies [44,47] was turned on to address the self-interaction error [48]. The long-range dispersion interactions were described by the Grimme’s D3 approach [49]. The structure of oxygen-terminated (1×3) $SrTiO_3$(110) surface was used to model the STO support. The Brillouin zone was sampled by a 2×6×1 k-point grid density. To study the generation of different active oxygen species on Ag/STO, several structures were considered: Ag overlayer films on STO(110) surface; Ag nanowire on STO(110) surface, clean STO (110) surface; pure Ag(100) and pure Ag(111) surfaces. Structurally, the key difference between the nanowire and film models is the lower coordination number of Ag atoms in nanowires as compared to films. More details were described in the Supporting Information.

To investigate the stability of different highly active oxygen species generated by the Ag/STO catalyst (O*, O_2, OH*, OOH* and H_2O), the binding energies of those species were calculated as the reaction energy expressed in Eq. (1):

$$* + \frac{y}{2}H_2O(g) + \left(\frac{x}{2} - \frac{y}{4}\right)O_2(g) \rightarrow O_xH_y^* \quad (1)$$

wherein *, H_2O(g) and O_2(g) are the clean surfaces, gas phases H_2O and O_2, respectively.

Besides, to understand the chemical interaction at the interface between Ag and $SrTiO_3$ and the electronic properties of Ag/STO interfacial sites at various distance from the STO support, the adhesion energies (ΔE_{adh}) were computed using the Eq. (2) and the charge density differences ($\Delta\rho$) were derived using the Eq. (3) for the Ag(100) overlayer films on STO (called as Ag_n/STO) with different Ag film thicknesses from one to four overlayers. The model of Ag(100) films is chosen due to its commensurate registry with the atomic arrangement on STO(110) substrate (Supporting Information, Figure S1 and Figure S2). The Bader charges were also calculated using the scheme developed in Henkelman et al. [50,51].

$$\Delta E_{adh} = \frac{E_{Ag_n/STO} - E_{STO} - nE_{Ag(g)}}{n} \quad (2)$$

where $E_{Ag_n/STO}$, E_{STO} and $E_{Ag_{gas}}$ are the total energies of Ag films supported on STO; clean STO and the one gas phase Ag atom, respectively.

$$\Delta\rho = \rho_{Ag_n/STO} - \rho_{STO} - \rho_{Ag_n} \quad (3)$$

where $\rho_{Ag_n/STO}$, ρ_{STO} and ρ_{Ag_n} are the charge densities of the Ag films on STO, clean STO and Ag_n cluster, respectively.

2.1.2. Optical simulations

To investigate the optical properties of $Ag/SrTiO_3$, we employ the optical package [52] implemented in the WIEN2k software package [53] and utilize the local orbitals (APW+lo) method coupling with the full potential (linear) augmented plane wave. We chose atomic sphere radii values of 2.37, 1.78, 1.61, and 2.36 a.u. for Sr, Ti, O, and Ag, respectively. The expansion of partial waves up to l_{max}= 10 inside the atomic spheres was used, and a cut-off $R_{MT}K_{max}$=8.0 with R_{MT}=1.61 a.u. was used to limit the number of plane waves. The Fourier-expansion was applied for charge density with G_{max}=20 Ry. The full Brillouin zone was sampled by a K-mesh of 2000 k-points or 3×25×25. The Sr 4 $s^2 4p^6 5 s^2$, Ti-3 $s^2 3p^6 3d^2 4 s^2$, O-2 $s^2 2p^4$, and Ag-4 $s^2 4p^6 4d^{10} 5 s^1$ were treated as semi-core states and were incorporated into the valence states. Absorption spectra of Ag nanoparticle supported on STO with different Ag particle sizes were investigated by numerical modelling using the procedure reported in our earlier studies [54–57].

2.2. Experimental details

2.2.1. Synthesis of $SrTiO_3$ perovskite (STO)

All analytical purity grade chemicals were obtained from Merck and used without further purification. The polymeric citrate precursor method was used to synthesize the $SrTiO_3$ perovskite. Typically, titanium isopropoxide with the amount of 0.568 g was dissolved in the volume of 5 ml ethylene glycol at room temperature for about 30 min. During the continuous stirring of the solution, citric acid with the weight of 4.201 g was added and stirred until completely dissolved. After that, the required amount of 0.422 g strontium nitrate (with the equal ratio 1:1 for Sr:Ti) was introduced gradually to the solution until obtaining the transparent solution. The mixture was kept at 70 °C for 2 h to ensure the complete dissolution of the reagents had reached. The reaction mixture then was heated at 120 °C for 5 h to facilitate the polymerization. After the solvents were heated and evaporated to form a transparent brown gel, it was subsequently calcined at 700 °C for 6 h to obtain the white-color STO powder.

2.2.2. Preparation of $Ag/SrTiO_3$ nanocomposites (Ag/STO)

The composites of metallic Ag and STO were fabricated via a room-temperature liquid-phase deposition approach. 0.5 g $SrTiO_3$ was dispersed into 30 ml deionized water under ultrasonic activation. After that, a chosen amount of $AgNO_3$ was introduced under stirring for 15 min. Next, 5 ml of glycol was added dropwise into the solution while keeping stirring. Subsequently, the mixture was stirred for 60 min continuously at room temperature. Finally, the products were centrifugated and washed with ethanol and deionized water three times, followed by the drying for 6 h at temperature of 60 °C. The final products were called as STO 0.5, STO 1.0, STO 1.5, STO 2.0, STO 3.0 and STO 5.0 according to the nominal weight ratio of Ag to $SrTiO_3$.

2.2.3. Catalyst characterization

The scanning electron microscopy (SEM) was used to study the morphology of the as-synthesized pristine STO and Ag/STO nanocomposites on an S4800 field emission scanning electron microscope (FESEM, Hitachi). A STADI-P x-ray diffractometer (STOE) was used to obtain the x-ray diffraction (XRD) patterns using monochromatic Cu-Kα radiation (λ = 1.5406 Å). A Thermo Fisher ESCALAB 220iXL with Mg-Ka radiation (1253.6 eV) was used to obtain the X-ray photoelectron spectroscopy (XPS) results and the Gaussian-Lorentzian fitting was applied for data processing. The XPS data was calibrated using the C1s peak at 284.8 eV.

Transmission electron microscopy (TEM) images were recorded at an acceleration voltage of 200 kV on a JEOL 2010. A JEOL JEM-ARF200F was used to receive the scanning transmission electron microscopy (STEM) images of the samples. Nitrogen adsorption and desorption investigation was carried out at 77 K on an ASAP 2010 sorption system, and the samples were pretreated by heating under the reduced pressure at temperature of 150 °C before the measurement.

2.2.4. Photocatalytic measurements

Rhodamine B (RhB) was used as a representative organic dye to evaluate the photocatalytic activities of the as-synthesized pristine $SrTiO_3$ perovskite and $Ag/SrTiO_3$ nanocomposites. The photodegradation of RhB was conducted in a 250 ml batch reactor, which could deliver a total power of 60 W light irradiation with the intensity of 3.2 mW/cm^2 by using the 4 UV–Vis solarium lamps (15 W, Philips). These UV–Vis solarium lamps could be controlled to generate both the UV range of sun light (wavelength range of 320–400 nm) and visible light spectra (wavelength range of 400–800 nm). The intensity of UV spectra is almost the same as the intensity of sun light radiation in a cloudy condition at the Baltic Sea, Rostock, Germany. To measure the radiation intensity, an UV light meter LT Lutron YK-35UV was used to capture the 290–390 nm spectral range.

Before starting the photocatalytic reaction, certain amounts of photocatalyst were suspended in 100 ml solution of RhB by constant stirring for 30 min in the dark to reach an equilibrium between adsorption/desorption. Subsequently, the UV light was turned on and the photoreaction was carried out for 90 min. During the process, 3 ml of the reaction solution was withdrawn every 15 min of time interval and centrifuged to remove the photocatalyst. Subsequently, the remaining solution was examined to detect the RhB concentration using the Shimadzu UV-2550, Japan. The photodegradation rate (%) was calculated using Eq. (4) as follows:

$$Photodegradation\ rate(\%) = \left(1 - \frac{C_0}{C_t}\right) \times 100\% \quad (4)$$

where C_0 and C_t are the initial concentration and the concentration of RhB at reaction time *t*.

3. Results and discussion

3.1. Electronic properties of Ag/STO interfacial sites

To understand the electronic interaction between the supported Ag nanoparticle and STO substrate and how the chemistries of Ag sites are modified upon supporting on STO, we analyze the Bader charges and the adhesion energies for the Ag films on STO with different Ag over-layer thicknesses. Those data are compared with the corresponding adhesion energy and Bader charge of surface Ag in the pure Ag(100) structure to demonstrate the change of Ag electronic properties in Ag/STO systems, as well as depicted for the range of influence from the STO substrate to the supported Ag particle. The models of Ag films supported on STO support with the Ag thickness ranging from 1 to 4 layers are presented in Fig. 1a-d. It should be noted that these models are used to evaluate the electronic properties of Ag atoms at different proximity from the STO surface; and how their chemistry was modified due to the interaction with the support. The thickness of Ag films in practical catalysts could be much larger (e.g. 7 nm Ag nanoparticle has ~28 Ag atomic layers). The charge density difference plots are also indicated in those figures to illustrate the charge transfer between Ag and STO. The computed adhesion energies and the charges of Ag atoms in those

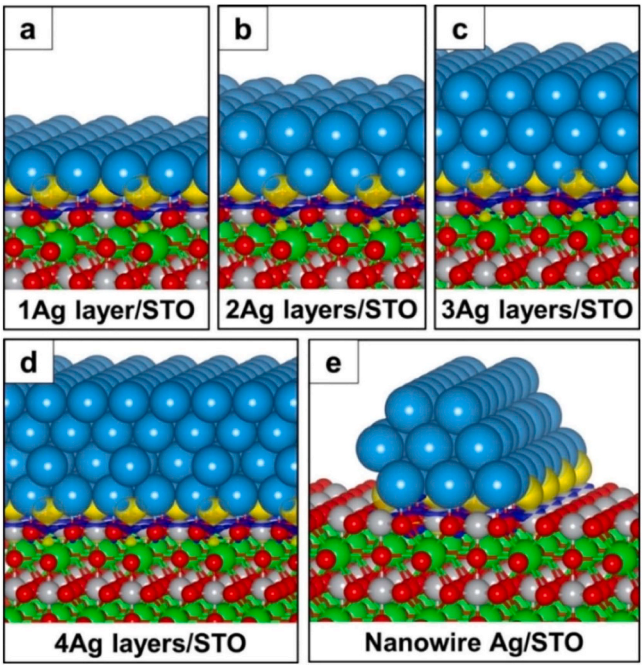

Fig. 1. Structures and charge density difference (CDD) plots for (a) one-layer Ag/STO; (b) two-layer Ag/STO; (c) three-layer Ag/STO; (d) four-layer Ag/STO and (e) nanowire Ag/STO. The dark blue and yellow regions represent the excess and depleted electron density zones, respectively. Ag, Sr, Ti and O are represented in light blue, green, grey, and red colours.

structures are shown in Table 1.

The computed adhesion energy of one Ag film on pure Ag(100) is −3.02 eV, and the surface Ag atoms have slight negative charge of −0.05 (Table 1). When one layer of Ag is supported on STO, the adhesion energy between them is −2.43 eV, and surface Ag atoms in the supported monolayer have a positive charge of +0.03. It is observed clearly in the charge density difference plot that the charges are transferred from an Ag monolayer to the STO substrate (Fig. 1a), where electron depletion regions (yellow color regions) are presented on the Ag layer, reflecting the positive charges have been induced on those Ag atoms. When the bilayer of Ag is supported on STO, the average adhesion energy is increased to −2.66 eV, and the differential adhesion energy (which is the binding energy of one more Ag layer on the existing monolayer) is −2.89 eV. The surface Ag atoms (in layer 2) have negative charges, consistent with the negative charge implemented on the surface Ag of pure Ag(100) structure (Table 1). Interestingly, Ag atoms in the first layer directly located above the STO surface still have positive charges of +0.04, suggesting the interaction between Ag and STO only locally affects the chemistry of Ag atoms in the narrow interface region of Ag/STO. The trends of adhesion energies and charges of Ag atoms for thicker structures of Ag overlayers on STO provide more understanding of the range of the interaction between supported Ag atoms and the STO substrate. The differential adhesion energies for adding one more Ag layer on existing Ag/STO for the 3-layer Ag/STO and 4-layer Ag/STO structures are −3.01 and −3.02 eV, respectively (Table 1). Those adhesion energies are almost the same as the adhesion energy for pure Ag(100) structure, reflecting that the bindings of an extra third Ag layer on the bilayer Ag/STO and fourth Ag layer on the tri-layer Ag/STO are similar to the binding of surface Ag layer to the underneath Ag layers in pure Ag(100). The computed Bader charge of surface Ag atoms in the 3-layer Ag/STO and 4-layer Ag/STO structures are also almost identical to the charge of surface Ag atoms on Ag(100) surface.

Table 1
Adhesion energy (eV) and Bader charge of Ag atoms for Ag films on STO.

Structures	Average/Differential adhesion energy	Charge of Ag atoms[a]	
Ag(100)	-3.02		-0.05
1 Ag layer on STO	-2.43		0.03
2 Ag layers on STO	-2.66/-2.89	Layer 1	0.04
		Layer 2	-0.02
3 Ag layers on STO	-2.78/-3.01	Layer 1	0.05
		Layer 2	0.01
		Layer 3	-0.04
4 Ag layers on STO	-2.84/-3.02	Layer 1	0.05
		Layer 2	0.01
		Layer 3	0.01
		Layer 4	-0.05

[a] Charges are computed as average Bader charge for all Ag atoms in the same layer. For different layers, layer 1 is the layer directly in contact with the STO support. The higher the index of the layer, the further it is from the STO. The highest index layer is the surface Ag layer.

Those observations therefore indicate that the chemistry of surface Ag atoms in the 3-layer Ag/STO and 4-layer Ag/STO structures are similar to surface Ag atoms of pure Ag(100) and the influence of STO to supported Ag atoms is narrowly confined at the Ag layer directly above the STO substrate, with some small residue is extended to the second layer above the interface. This similar phenomenon has also been observed for other supported metal nanoparticle systems such as Au/InP [37], Au/Fe_2O_3 [36], M/TiB_2 (M=Ag, Au, Pd and Pt) [58] and Cu/amorphous carbon [35] reported recently. It is clearly illustrated in the charge density difference plots for the 2, 3 and 4-layers of Ag films on STO (Fig. 1b-d), showing that the charge transfer processes are mainly localized within the interface between STO substrate and the first Ag layer above the substrate, inducing positive charge for Ag atoms at that location.

Since the charge transfer between STO and Ag is confined only within two layers above the substrate and Ag atoms beyond 3 layers from STO are similar to Ag atoms of pure Ag(100), we create the model of Ag nanowire on STO substrate (Fig. 1e) to study the adsorption and activity of oxidizing agents at the interface. This model includes 3 layers of Ag above the STO with the interface regions having both STO sites and Ag sites. The charge transfer between the supported nanowire Ag particle and STO is also similar to the overlayer films (Fig. 1e). Due to the presence of both sites from the STO substrate and the active sites of supported Ag nanoparticle at the interface, this model is very convenient in evaluating the synergistic role of the substrate and supported metal sites in facilitating the adsorption and activation of reactants at the interface.

3.2. Adsorption and activation of oxidizing agents at Ag/STO interface

Next, to demonstrate the importance of Ag/STO interactions to the catalytic activity, we evaluate the adsorption of reactive oxygen species on different active sites. To be photo-catalytically effective, Ag/STO should be able to generate a high density of active reagents for the photocatalytic reaction. Due to the target reaction being the oxidized-degradation of RhB, we computed the adsorption energy of key possible oxidizing agents, including O_2, H_2O, OOH*, O* and OH* on STO (110) surface (represents the clean STO substrate), clean Ag(111) surface (represents the unsupported Ag metal sites), a monolayer Ag supported on STO and at the Ag/STO interface of the nanowire model. The results are presented in Fig. 2a.

Molecular O_2 adsorbs weakly on Ag(111) surface with the binding energy of −0.3 eV, consistent with the value reported in earlier studies [59]. On the monolayer Ag/STO, the binding energy of O_2 is slightly stronger with the values of −0.7 eV, maybe due to the positive charge implemented on the Ag site of the monolayer Ag/STO. The stronger binding energy of adsorbate on positively charged metal sites has recently been reported for Au/Fe_2O_3 and Au/InP systems [36,37]. Interestingly, STO is unable to adsorb O_2, consistent with the reported inert nature of STO with O_2 adsorption and activation [43,60].

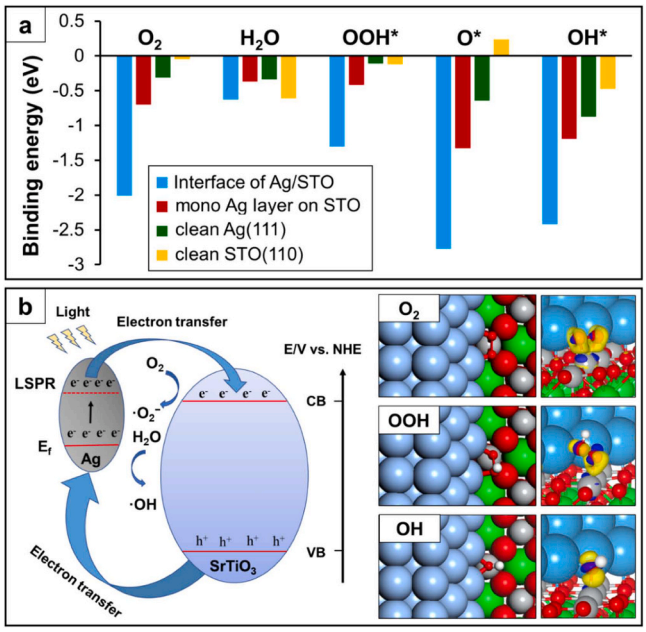

Fig. 2. (a) Binding energies of oxidizing agents (O_2, H_2O, OOH*, O* and OH*) at the interface of Ag/STO; on a monolayer of Ag/STO; on clean STO(110) and on clean Ag(111) surface; (b) The Local Surface Plasmonic Resonance (LSPR) between Ag/STO. Structures and charge density differences for reactive species (O_2, OOH and OH) at Ag/STO interfacial sites.

Surprisingly, O_2 adsorbs very strongly at the interface of Ag/STO by forming the bonds with both Ag sites and STO (Fig. 2b), resulting in a strong adsorption energy of −2.02 eV at the interface. In the charge density difference plot for adsorbed O_2 at the Ag/STO interface, high densities of electron are accumulated along the Ag-O bonds and Ti-O bond (bonding with STO substrate), demonstrating the synergistic role of metal and STO sites in stabilizing the adsorbed O_2 molecule at interfacial sites. The unprecedented strong adsorption of O_2 at the interface of Ag/STO suggests that it might be an important oxidizing agent to facilitate the photo-degradation of RhB compound.

In contrast to the trend of O_2 adsorption, water molecules adsorb weakly on all 4 surfaces via the van der Waals interaction. The binding energies of water with 4 surfaces vary narrowly within the range from ~0.4–0.6 eV (Fig. 2a). Due to its low sticking possibility, water is unlikely a direct oxidizing agent. However, other oxygen-derivatives from water and O_2, including O*, OH* and OOH* (* denote the adsorbed state), all adsorb much stronger at the Ag/STO interface than on pure STO and clean Ag(111) surfaces (Fig. 2a). This observation demonstrates the crucial role of the interfacial sites in generating and stabilizing those high active oxygen species. Indeed, the computed binding energies of O*, OH* and OOH* on the Ag/STO interface are strengthened by 1.8 eV, 1.4 eV and 1.0 eV, respectively, compared to the corresponding values of those species on pure Ag(111) surface (Fig. 2a). Those observations therefore suggest that those active oxygen species could feasibly participate in the oxidation of RhB compound at the Ag/STO interface.

The widely proposed mechanism of the LSPR-mediated charge transfer occurring between $SrTiO_3$ and Ag, and how the oxidizing agents are generated on this catalyst are presented in Fig. 2b. When the Ag/$SrTiO_3$ nanocomposite is activated with light irradiation having the wavelengths overlapping with the plasmon frequency of Ag nanoparticles, there occurs the generation of energetic electrons which could overcome the Schottky barrier at the interface of Ag/STO and are simultaneously transferred to the conduction band (CB) of $SrTiO_3$ [61]. Part of these electrons are accumulated at interfacial Ag/STO sites and interact with adsorbed oxygen stabilizing at the interface to produce $^*O_2^-$ species. Adsorbed H_2O molecules could also be activated at the Ag/STO to produce OH* or OOH* species. The structures of O_2*, OH* and OOH* adsorbed at the interface of Ag/STO are shown as insets in Fig. 2b. Charge density difference plots for those structures also show the corporative role of metal site and STO substrate site in stabilizing those oxygen species. The computed Bader charge indicates that upon adsorption at the interface of Ag/STO, the charge of adsorbed O_2 is −1.13 e, consistent with the proposed active O_2^- species in the photo-oxidation mechanism (Fig. 2b). Therefore, those highly active oxygen species (including O_2^-, OH and OOH) are proposed as active oxidizing agents facilitating the degradation of RhB. At the same time, electrons on the valence band (VB) of STO also move back to the Ag nanoparticles to maintain the electric neutrality, creating behind the holes (h^+) that could also participate in the photoreactions. The role of the h^+ in the photodegradation of Rhodamine B will be evaluated later in Section 3.5.3.

Finally, the activation barriers for the generation of those active oxygen species are computed on clean Ag(111), STO and Ag/STO (Fig. 3). On both Ag(111) and STO(110) surfaces, the direct activation of O_2 generating atomic oxygen is difficult with extreme high barriers of 1.21 and 1.44 eV, respectively. The activation of water forming hydroxy group is also not feasible with high barriers of 1.97 and 1.11 eV on Ag (111) and STO(110) surfaces. Those high barriers for both O_2 and H_2O activations on Ag(111) and STO(110) surfaces suggest that metallic Ag sites or STO sites separately are not active in generating the highly active oxygen species which are crucial for the photo-oxidation reactions. The computed barriers in this study are greatly consistent with low activity for Ag and STO towards O_2 activation and H_2O activation reported in the literature [62].

However, at the interface, the formations of those active oxygen species are much more feasible, except for the direct dissociation of O_2. Despite adsorbing strongly, breaking the O-O bond from adsorbed O_2 molecule into two atomic oxygens at the Ag/STO interface is quite difficult with high computed barrier of 1.25 eV (Fig. 3a), ruling out the contribution of O* as an oxidizing agent in the photo-oxidation reactions. Water molecule adsorbs slightly stronger at Ag/STO interfacial

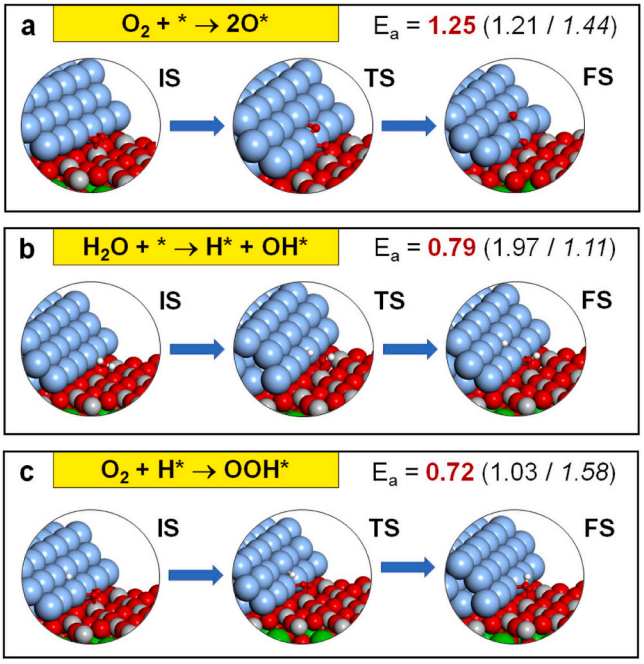

Fig. 3. Activation of O_2 (a) and H_2O (b) and the formation of OOH (c) at the interface of Ag/STO. IS, TS and FS denote for the initial, transition and final states, respectively. The activation barrier (in eV) for those reactions are presented in **bold values**, while value in parentheses are activation barriers of the same reaction on pure Ag(111) surface (regular values) and on clean STO(110) surface (*italic values*).

sites with a binding energy of −0.61 eV (vs −0.34 eV on Ag(111) surface), but it can be activated with a barrier of only 0.79 eV, producing OH* strongly adsorbs at the interface and H* adsorb on metal Ag sites (Fig. 3b). The kinetically feasible formation of OH* at the Ag/STO interface indicating that it might be an important oxidizing agent for Ag/STO and is consistent with the mechanism proposed in Fig. 2b. Furthermore, H* generated form H_2O activation can react with the adsorbed O_2, forming adsorbed OOH* also strongly stabilize at the interface. The activation barrier for OOH* formation is only 0.72 eV (Fig. 3c). Once OOH* is formed, it could easily react with H* to form two OH* species via a low barrier reaction [36]. Therefore, the presence of OOH* at the Ag/STO interface might be low. From those kinetic data, we could propose that O_2 and OH* are likely the active oxidizing agents presented at the Ag/STO interface to facilitate the photo-degradation of RhB. The formation of OH* at the interface could be from two routes: the direct H_2O splitting route and the indirect route from O_2 via OOH* intermediate. The obtained results also emphasize the important role of interfacial sites via the synergistic participation of both Ag site and STO sites in generating and stabilizing those active oxidizing agents, which are crucial for the oxidation-degradation reactions.

3.3. Optical properties of Ag/STO

The optical properties of Ag/STO catalyst are another crucial factor contributing to the activity of the photocatalyst. STO perovskite alone only can adsorb UV light with a wavelength smaller than 400 nm. Ag nanoparticle supported on STO was able to adsorb light in the visible range (400–700 nm) via the localized surface plasmon resonance (LSPR) as was reported in the literature [15,63,64], making Ag/STO more practical applicable photocatalysts. In this part, we investigate in more detail the influence of Ag dosage and the Ag nanoparticle size on the optical properties of Ag/STO to establish the strategy for designing efficient Ag/STO photocatalysts.

Firstly, to understand the LSPR occurring when an Ag nanoparticle is supported on STO, we simulate the optical conductivities at different wavelengths by the WIEN2K package using the structure models of Ag

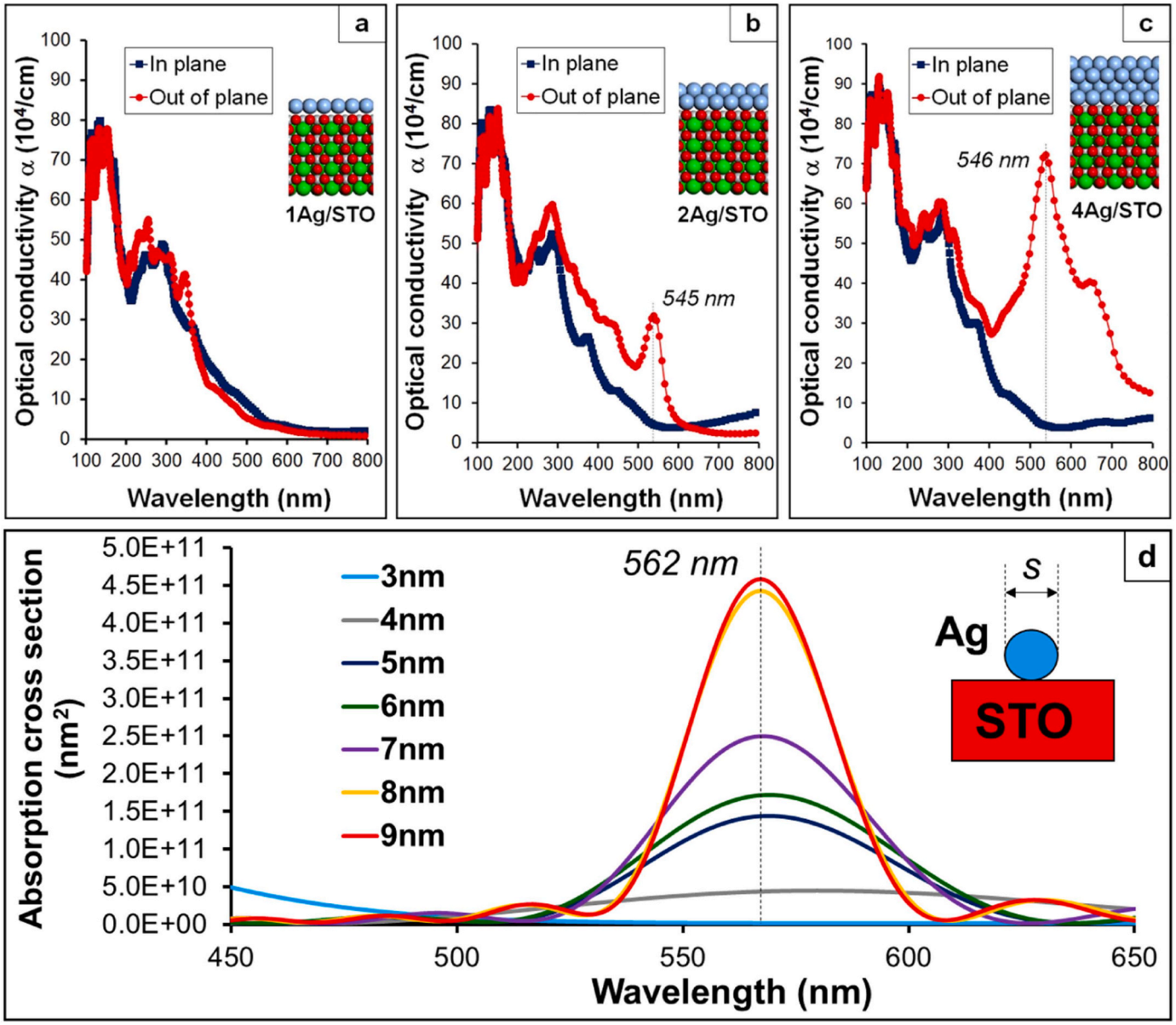

Fig. 4. Absorption spectra of overlayer Ag films supported on STO with different number of Ag layers: a) a monolayer of Ag supported on STO; b) a bilayer of Ag supported on STO and c) a four-layer of Ag supported on STO substrate. (d) Absorption spectra of Ag nanoparticle supported on STO with different Ag particle size (*s*) ranging from 3 to 9 nm. The spherical Ag particle support on the STO substrate is also illustrated.

overlayer films on STO (illustrated in Fig. 1). As shown in Fig. 4a, there is no absorption peak for wavelengths in the range of 400–700 nm when a monolayer Ag is supported on STO, indicating the LSPR has not been triggered for this structure. Interestingly, the LSPR phenomena occurs for thicker structures of Ag films supported on STO (Figs. 4b and 4c). Indeed, there is an appearance of a peak at 545 nm in the simulated spectra of the bilayer Ag/STO structure, suggesting that the bilayer Ag/STO is ready to adsorb visible light. However, the intensity of this absorption peak at 545 nm for the bilayer Ag/STO is quite weak (Fig. 4b). For a thicker system 4-layers Ag/STO composite, the intensity of absorption peak at 546 nm is significantly stronger (Fig. 4c), indicating the higher efficiency of this system to absorb visible light and therefore can be more adequately used in photo-catalytic reactions. The observed trend shows that to induce the LSPR on the Ag/STO catalyst and enable it to absorb visible light, a high Ag dosage needs to be used to form thick enough Ag layers on the STO substrate.

Next, we investigate the influence of Ag nanoparticle size on the optical property of Ag/STO. Since it is very challenging to study the large Ag nanoparticle (> 3 nm) at the DFT level due to the high computational cost, we adopt the numerical approach which was applied in our earlier studies [54–57]. Indeed, the 3 nm Ag nanoparticle model with the truncated octahedral shape has ~1300 atoms, and to model the 8-nm-size particle, the cluster containing ~23,000 atoms should be used, making it impossible for DFT calculations to be performed for those systems. Using a numerical approach, we are able to simulate the absorption spectra for the Ag spherical nanoparticle supported on STO with particle size (l) ranging from 3 to 9 nm. The absorption spectra at different particle sizes are presented in Fig. 4d. It is found that the absorption peak at 562 nm appears in all absorption spectra when the Ag particle increases from 4 to 9 nm. The close value of absorption peak using the numerical approach (562 nm) with the value obtained from DFT calculations (546 nm) again confirms the LSPR phenomena has occurred on the Ag/STO composites. Furthermore, the numerical calculations could provide quantified information on the variation of the absorption peak intensities versus different Ag particle sizes. The 4 nm Ag/STO is only able to absorb the wavelength 562 nm with low intensity. The larger the Ag particle, the stronger the absorption intensity (Fig. 4d). However, the intensity of the 562 nm absorption peak for the 8 nm and 9 nm Ag particles are very close, suggesting that the effect of Ag particle size on the LSPR phenomena might reach a saturation at those sizes.

3.4. Strategy to design Ag/STO for maximize photocatalytic activity

Those detailed insights into the interfacial activities and optical properties are key to the design of efficient Ag/STO catalysts in photo-oxidation reactions. There are two key factors contributing to the high activity of Ag/STO photocatalysts: 1) the feasibility of generating high oxygen species that are active agents for oxidation reactions, and 2) the ability to absorb visible light with adequate intensity. To facilitate the former factor, maximum exposure of interfacial sites should be promoted. It could be done by controlling the dosage of Ag amount. If the Ag dosage is too high, then Ag atoms are nucleated to form larger particles that partially cover the STO substrate, reducing the exposure of interfacial sites [58]. The amount of Ag should be controlled to form smaller Ag particles and thus optimize the number of exposed interfacial sites which are active sites generating high active oxygen species for the photo-oxidation reactions.

However, the optical property of Ag/STO is sacrificed if the Ag particle size is smaller than 4 nm, as has been analyzed in detail in Section 3.3. To enable Ag/STO to absorb visible light with strong intensity, thick enough Ag layers need to be formed above the STO and the Ag particle size needs to reach a certain large value (> 5 nm). Therefore, to design an efficient Ag/STO catalyst for photo-oxidation reactions, we need to compromise both the exposure of interfacial sites and the optical property of the catalyst by controlling and optimizing the dosage of Ag. From the results above, Ag particle sizes from 5 to 7 nm are predicted to be the best. Subsequent sections will present experimental results that validate this theoretical prediction.

3.5. Preparation of Ag/STO nanocomposites and their photocatalytic activities

3.5.1. Synthesis of Ag/STO nanocomposites with different Ag loadings

As suggested by theoretical prediction, the Ag/STO nanocomposites with different Ag dosages of 0.5 wt%, 1.0 wt%, 1.5 wt%, 2.0 wt%, 3.0 wt% and 5.0 wt% were synthesized to find the optimum loading amounts given the highest catalytic activity. The XRD patterns of pristine $SrTiO_3$ and Ag/$SrTiO_3$ nanocomposites at different amounts of Ag are presented in Fig. 5. The peaks located at 22.8°, 32.5°, 40.0°, 46.6°, 52.5°, 57.9°, 68.0° and 77.4° in the XRD pattern of STO can be well-indexed to diffraction peaks of (100), (110), (111), (200), (210), (211), (220) and (310) planes of $SrTiO_3$ cubic phase (JCPDS card No. 35–0734) [65], suggesting that pure $SrTiO_3$ phase has been well crystallized. Upon loading with Ag nanoparticles, those characteristic diffraction peaks of $SrTiO_3$ are still presented in the XRD patterns of all Ag/$SrTiO_3$ nanocomposites (Fig. 5), showing that there is no change in the structure of $SrTiO_3$ phase. Careful observation reveals that there are no changes of those dominant XRD peaks of STO after loading with Ag. The computed lattice parameters of Ag/STO nanocomposites before and after loading with Ag are almost unchanged (Table T1, Supporting Information), ruling out the possibility of Ag incorporation into the $SrTiO_3$ crystal lattice and suggest that Ag atoms are nucleated on the surface of STO forming metallic Ag nanoparticles. At higher Ag-loaded samples, there is the presence of a characteristic peak of metallic Ag in the XRD patterns. The inset picture in Fig. 6 shows the formation of the metallic Ag phase when the Ag loading is larger than 2.0 wt%, evidenced by the appearance of the peak located at 38.45° corresponds to the Ag(111) plane [66]. The intensity of this peak is stronger with increasing Ag loadings, reflecting the higher crystalline of metallic Ag with larger Ag particle size. It is consistent with the prediction in the design strategy section discussed above.

3.5.2. Activity of Ag/STO with different Ag loadings in RhB photo-degradation

The photocatalytic efficiencies of the synthesized Ag/STO samples with different Ag loadings are tested in the photodegradation under sunlight irradiation of an organic pollutants in wastewater due to their practical applications and convenience of catalytic evaluation. Rhodamine B (RhB) is chosen as a model compound for hazardous organic pollutants in this work. First, we check whether the Ag/STO can absorb visible light and how effective it is in the RhB photo-degradation, using the Ag/STO sample with 1 wt% of Ag (named STO 1.0) as the representative sample. The time-dependent UV–vis spectra of

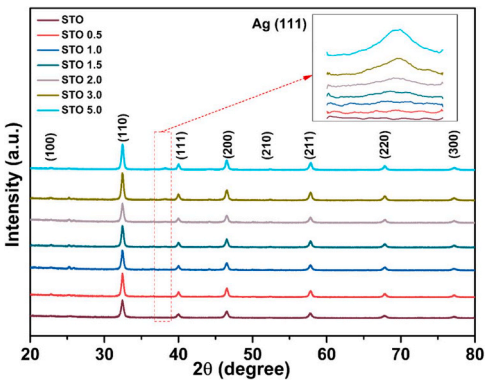

Fig. 5. XRD patterns of pristine STO and Ag/STO samples with different Ag loadings.

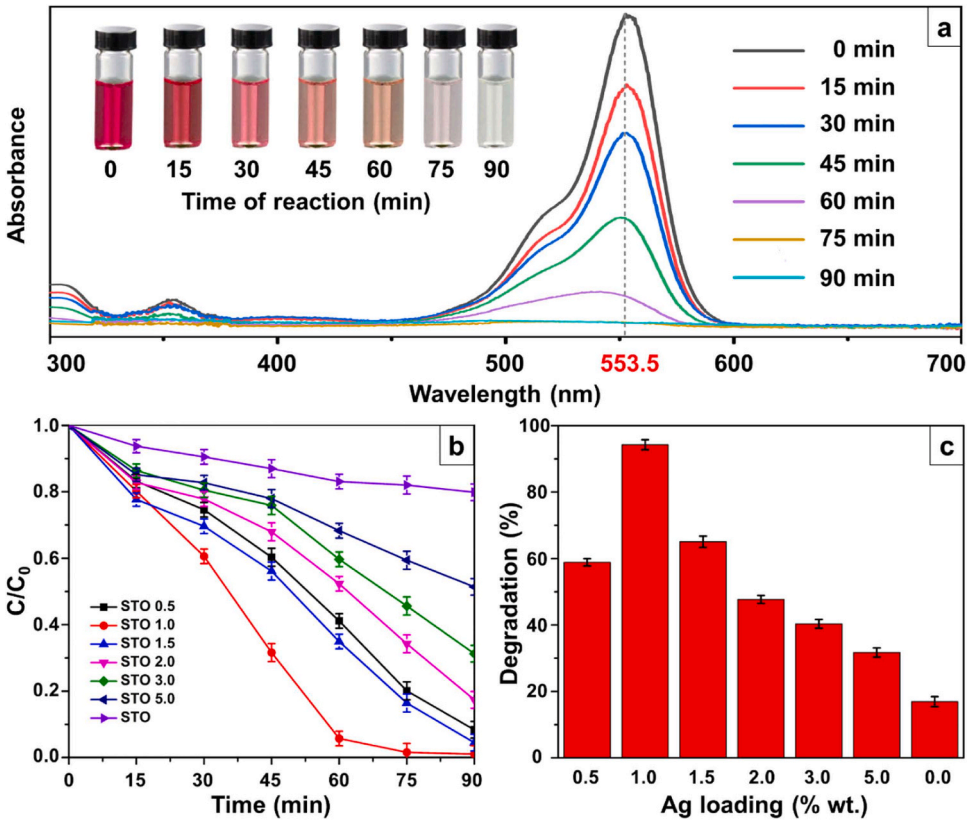

Fig. 6. (a) Time-dependent UV–vis spectra of RhB degradation on STO 1.0. Reaction conditions: 50 mg of catalyst loading and 100 ml of 10 ppm RhB solution. Inset shows the change of solution colors over the course of photocatalytic reaction. (b) Time-dependent photocatalytic activity of different Ag/STO samples in RhB degradation. (c) Photodegradation rate of RhB over Ag/STO catalysts with different Ag loadings after 60 minutes of reaction.

photodegradation of RhB on STO 1.0 is presented in Fig. 6a. The STO substrate without Ag is not able to absorb visible light [67]. However, upon the deposition of Ag nanoparticle on STO, the composite is predicted to be visible light active as was predicted by our theoretical investigations. Indeed, the intensity of absorption peaks at 553.5 nm of RhB in the UV–vis spectra decreased during the photodegradation process as presented in Fig. 6a, and 95 % of RhB degradation rate was achieved after 90 min (Fig. 6b), demonstrating the high efficiency of Ag/STO as photocatalyst for RhB degradation under visible light irradiation.

Next, to validate the catalyst designing strategy proposed by theoretical studies in Section 3.4, the photocatalytic activities of Ag/STO with different Ag loadings are examined in Figs. 6b and 6c. RhB is unable to be decomposed under visible light irradiation without the catalyst [68]. However, in the simultaneous presence of photocatalysts and visible light, RhB was easily degraded. Pure STO is unable to absorb visible light due to a wide band gap energy [69] and has low activity toward RhB degradation with only ~18 % of RhB is eliminated after 1 h of reaction time (Fig. 6c). Upon loading STO with Ag, all the Ag/STO samples possess much higher photocatalytic efficiency than pure STO, emphasizing the role of supported Ag nanoparticle in boosting the activity (Fig. 6b). However, there is an optimum amount of Ag loading in the activity trend of Ag/STO samples as is shown in Fig. 6c. The STO 1.0 photocatalyst (prepared with 1 % wt. Ag) has the highest photocatalytic activity, and the RhB degradation rate on STO 1.0 reaches 92.8 % after 1 h of reaction time. Both lower dosage and higher dosage of Ag result in the decreasing of Ag/STO photocatalytic activity. The corresponding degradation rates of RhB after 1 h of reaction time on STO 0.5 and STO 1.5 are 59 % and 65 %, respectively. This observation excellently validates the designing strategy guided by our theoretical studies. The STO 1.0 has the highest activity due to its best adequacy in balancing both the optical property and the exposure of interfacial active sites between Ag and STO. The loading of 1 % wt. of Ag in STO 1.0 is large enough to enable the catalyst absorbing visible light with strong intensity, but in the meantime is also not too high to ensure the high density of exposed Ag/STO interfacial sites.

3.5.3. *Trapping experiment to identify active oxidizing agents on Ag/STO*

The above-mentioned data and analyses confirm that the coupling of the metallic Ag phase onto the surface of STO improves the photocatalytic activity of Ag/$SrTiO_3$ catalysts. Next, we investigate in more detail the reactive species which play the key roles in the photodegradation of RhB. DFT calculations in Section 3.2. have identified potential active oxygen species generating at the Ag/STO interface, including adsorbed O_2 and OH*. Besides, as proposed in the mechanism of LSPR, the holes forming on the STO substrate might also participate in the photoreaction as well (Fig. 2b). To shed light in identifying the nature of active oxidizing agents, the impact of main reactive species involving superoxide anion radicals ($\bullet O_2^-$), the holes (h^+) and hydroxyl radicals (•OH) in the photodegradation of RhB under solarium irradiation on STO 1.0 catalyst are investigated via radical trapping experiments.

To understand the impact of these reactive species, the photodegradation of RhB was tested of STO 1.0 with the addition of various scavengers, including ethylene diamine tetra-acetic acid (EDTA) to scavenge the holes activities, the tert-butyl alcohol (t-BuOH) to quench the •OH radicals and benzoquinone (1,4 BQ) as $\bullet O_2^-$ scavenger. As can be seen in Fig. 7, the degradation efficiency of STO 1.0 is significantly inhibited after the addition of 1,4 BQ, indicating that $\bullet O_2^-$ is one of the major reagents responsible for the decomposition of RhB. Similarly, upon the introduction of t-BuOH as an efficient scavenger of •OH, the degradation rate of RhB is sharply reduced from 98 % (with no

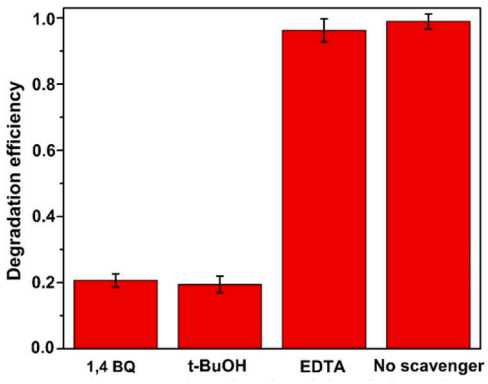

Fig. 7. The aqueous phase photodegradation of RhB on the STO 1.0 nanocomposite sample with the presence of different scavengers, including benzoquinone (1,4 BQ); tert-butyl alcohol (t-BuOH) and ethylene diamine tetra-acetic acid (EDTA). Reaction condition: catalyst loading: 50 mg, RhB solution: 100 ml, concentration: 10 ppm, scavengers' concentration: 1 mmol L^{-1}.

scavenger) to 18 % (with the presence of t-BuOH). These observations confirm that the photogenerated $\bullet O_2^-$ and •OH play crucial roles in the degradation of RhB, in excellent agreement with the prediction made by the DFT calculations. Contrarily, only a negligible decrement in the rate of RhB degradation (~3 %) is observed after adding EDTA, suggesting that holes (h^+) do not participate in the photo-degradation of RhB and is also consistent with the study by Wu et al. [70]. The importance of $\bullet O_2^-$ and •OH in facilitating the oxidation-degradation of RhB detected in trapping experiments is excellently consistent with the prediction of DFT calculations in Section 3.2. This observation again demonstrates the capabilities of theoretical investigation not only in providing the designing strategy to achieve high photocatalytic efficiency but also in identifying potential reactive species during the photocatalytic reaction on the Ag/STO nanocomposite.

3.6. Characterization and stability test of the optimum Ag/STO catalyst (STO 1.0)

3.6.1. Catalyst characterization

The photocatalytic testing of Ag/STO with different Ag loadings in RhB photo-degradation in Section 3.5 revealed that STO 1.0 has the highest photocatalytic activity. Therefore, this sample will be further characterized to evaluate its electronics properties, and its reusability will be comprehensively examined. The size and morphology of the pristine STO and the STO 1.0 samples were analyzed by the SEM images (Fig. 8a, b). The pristine STO has a dense structure and consists of spongious agglomerates which are characterized by a closed microporosity. The surface of pristine STO is rough, showing organized worm-shaped agglomerated with a 2D distribution (Fig. 8a). The mesoporous structure and the worm-shaped morphology in still maintained in the SEM image of STO 1.0 (Fig. 8b), consistent with the analysis from N_2 adsorption test and surface areas measurement (Supporting Information).

The structure of STO 1.0 is further examined by TEM image (Fig. 8c, d). In the low-resolution TEM image (Fig. 8c), relatively uniform distribution of Ag nanoparticles was observed. The HRTEM image on the Ag/STO 1.0 sample shows two characteristic lattice fringes (Fig. 8d). The first lattice fringe has a *d*-spacing of 0.28 nm which corresponds to the (110) plane of cubic $SrTiO_3$ [71]. Another lattice fringe with a *d*-spacing of 0.23 nm is characteristic of the (111) plane of face-centered-cubic Ag [72], demonstrating the formation of heterostructure between metallic Ag and $SrTiO_3$. The particle size distribution of metallic Ag is presented as inset in Fig. 8c, showing the average size of Ag of the STO 1.0 sample is around 6.24 ± 0.07 nm. At this particle size, high intensity of the wavelength 562 nm can be absorbed by the STO 1.0 sample as was revealed by numerical simulation in Fig. 4d. The dosage 1 % wt. of Ag is not too large to generate high density of interfacial sites, reflecting from the distribution of uniform Ag particles on STO (Fig. 8c). Higher Ag dosages result in the formation of larger Ag particle, as could be observed from the higher intensities of Ag(111) signal in the XRD

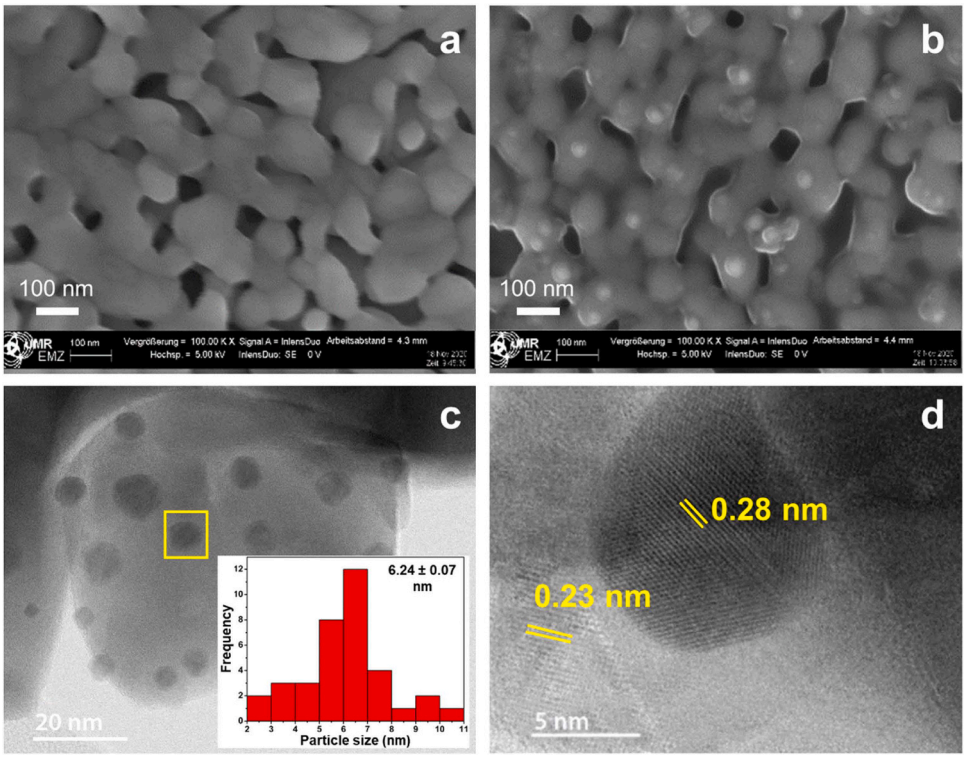

Fig. 8. SEM images of STO (a) and STO 1.0 (b). (c) Low-resolution TEM image of STO 1.0. Inset: histogram of the particle size distribution of metallic Ag. (d) High-resolution HR-TEM image of STO 1.0.

patterns for STO 3.0 and STO 5.0 (Fig. 5), reducing the exposure of interfacial sites. Indeed, the particle size for Ag/STO nanocomposite with 5 % wt. of Ag loading (STO 5.0) is calculated of ~9.8 nm using the Debye-Scherrer equation. It emphasizes again the designing strategy that the optimum Ag loadings need to be controlled to compromise both the density of interfacial sites and the optical property for Ag/STO composites.

To understand more about the electronic properties of STO 1.0 and the surface characteristics, XPS analysis is carried out (Fig. 9). The C 1 s XPS peak is assigned to adventitious carbon presented on the material surface [73]. In the Sr 3d spectra (Fig. 9a), the XPS peaks at 132.71 eV and 134.45 eV can be assigned for Sr $3d_{5/2}$ and Sr $3d_{3/2}$ of Sr^{2+} oxidation state [74]. The Ti 2p XPS binding energies at 463.56 eV and 457.87 eV (Fig. 9b) are characteristic of Ti $2p_{1/2}$ and Ti $2p_{3/2}$ peaks of Ti^{4+} state, respectively [74]. The O 1 s spectra exhibits three binding energies of 529.10, 531.28 and 532.31 eV (Fig. 9c), the two former peaks are assigned for the lattice O^{2-} and surface hydroxyl, and the last peak corresponds to the chemical adsorbed oxygen [48,75,76]. The two peaks centered at 367.34 and 373.36 eV in the Ag 3d spectra (Fig. 9d) are assigned to metallic states Ag $3d_{5/2}$ and Ag $3d_{3/2}$ of the Ag/$SrTiO_3$ heterostructure [77], confirming the successful nucleation of Ag nanoparticle on the surface of STO in the as-synthesized STO 1.0 sample.

3.6.2. *Stability testing*

Another important factor for the practical applications of a photocatalyst is its stability. To evaluate the reusability of Ag/$SrTiO_3$ nanocomposites, recycling test was conducted for four experimental cycles on STO 1.0 photocatalyst. The stability testing results are presented in Fig. 10a. It is observed that the activity of the STO 1.0 is stable after four recycles of RhB photodegradation without any significant loss in the activity, emphasizing that the synthesized Ag/$SrTiO_3$ nanocomposites can be used for practical photocatalytic degradation of pollutant compounds in a long run. The structure of the spent STO 1.0 catalyst is further examined by its XRD patterns (Fig. 10b) and HAADF-STEM images (Figure S5, Supporting Information). After finishing 4 cycles of photocatalytic degradation of RhB, the structure of spent STO 1.0 is almost unchanged compared with the XRD pattern of the fresh sample (Fig. 10b). All characteristic peaks for fresh and spent STO 1.0 samples are identical, revealing the good stability of the Ag/STO structure under the photocatalytic operation conditions. The HAADF-STEM images also confirm the presence of Ag nanoparticle and the Ag(111) lattice fringe after the stability test, in excellent consistent with the XRD analysis (Figure S5, SI).

4. Conclusions

In this study, the insight into the photocatalytic activity of Ag/$SrTiO_3$ nanocomposites was investigated using the combination of theoretical and experimental approaches. Different levels of theoretical investigations, including atomic-scale Density Functional theory (DFT) calculations, full potential augmented plane wave optical simulations and particle-scale numerical simulations were used to gain insights into the activity of interfacial sites between Ag/STO and the influence of Ag particle size to the optical properties of the nanocomposite. It was identified that interfacial sites had high activity in generating the reactive oxygen species, O_2 and OH, which were crucial for the oxidation-degradation of RhB. Besides, in order to induce the Localized Surface Plasmon Resonance and enable the Ag/STO material to absorb visible light with high intensity, the Ag particle had to reach certain large size. This information from theoretical studies was used to suggest the design strategy for Ag/STO by carefully controlling the Ag dosage. Comprehensive experiments were conducted to validate the theoretical prediction by preparing Ag/STO composites with different Ag content varying from 0.5 to 5 wt%. The as-synthesize Ag/STO nanocomposites

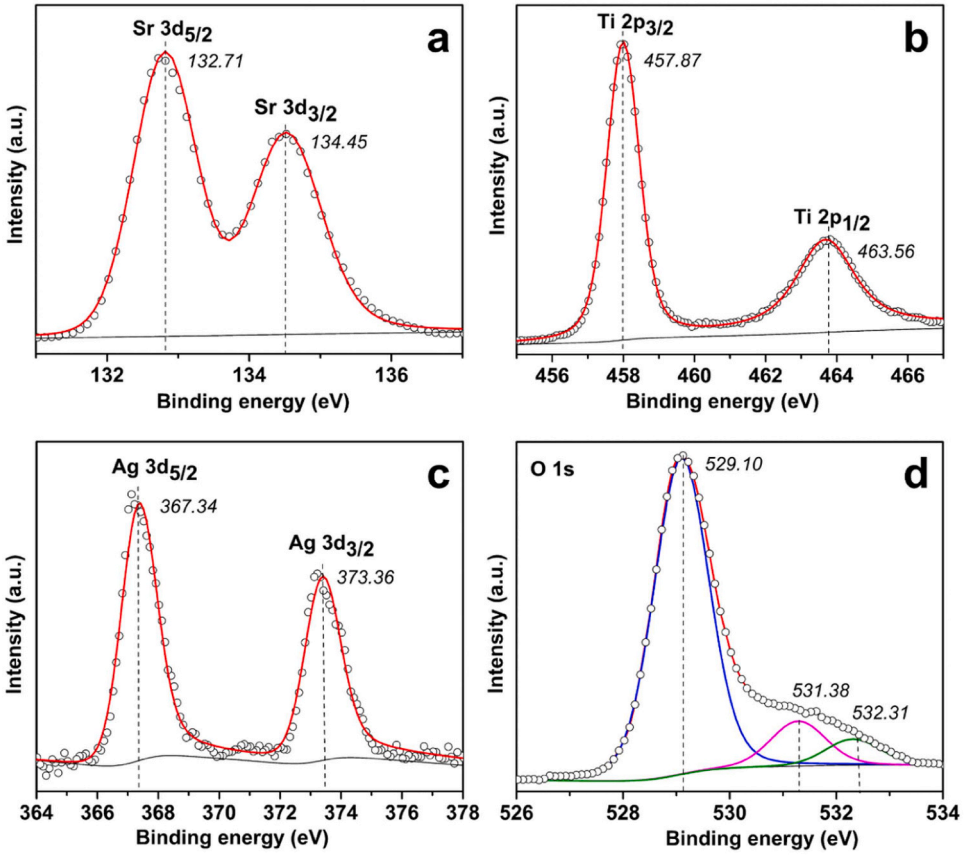

Fig. 9. High-resolution XPS spectra of the Sr 3d peaks (a), Ti 2p peaks (b), Ag 3d peaks (c) and O 1 s peaks (d).

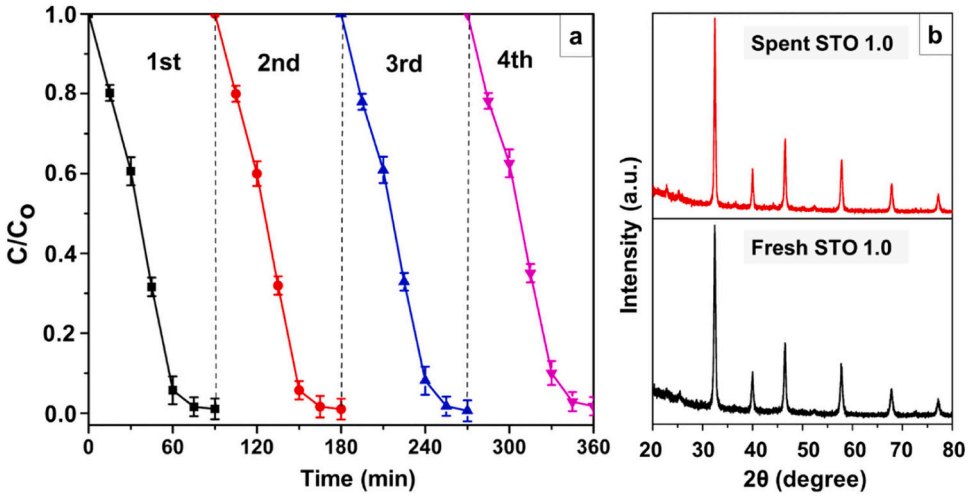

Fig. 10. (a) Reusability of STO 1.0 sample in four recycling tests for the photocatalytic degradation of RhB. Reaction condition: Catalyst loading: 50 mg, RhB solution: 100 ml, concentration: 10 ppm. (b) XRD patterns of fresh STO 1.0 before photocatalytic degradation of RhB and spent STO 1.0 after 4 cycles of photocatalytic degradation of RhB.

possessed much higher activities than the pure STO for the photodegradation of RhB under solarium irradiation, and the photocatalytic rates of Ag/STO varied significantly with the loadings of Ag with the optimum activity reached at Ag loading of 1 % wt., excellently confirmed the capabilities of theoretical prediction. Quenching experiments also detected that the generated •OH and $\bullet O_2^-$ species were the major reagents responsible for the photodegradation of RhB on the Ag/$SrTiO_3$ catalyst, which were exactly identified from the DFT calculations. This work demonstrated that the surface modification strategy is very helpful in designing and developing advanced photocatalysts for the environmental remediation purposes. The integration between theoretical and experimental approaches in this study provides a framework to design efficient photocatalysts for other applications such as CO_2 photo-reduction; H_2O photo-splitting or for photo-organic synthesis.

CRediT authorship contribution statement

Hendrik Kosslick: Methodology. **Khuong Phuong Ong:** Methodology, Investigation. **Nam-Trung Nguyen:** Writing – review & editing, Supervision, Funding acquisition. **Thi To Nga Phan:** Writing – original draft, Visualization, Methodology, Investigation, Formal analysis, Data curation, Conceptualization. **Pham Thanh Huyen:** Writing – review & editing, Supervision, Funding acquisition. **Tuyen Le Van:** Writing – original draft, Visualization, Methodology, Investigation, Formal analysis, Data curation. **Jia Zhang:** Writing – review & editing, Supervision, Funding acquisition. **Quang Thang Trinh:** Writing – original draft, Visualization, Methodology, Formal analysis, Data curation. **Jun Zhang:** Investigation. **Tuan-Khoa Nguyen:** Investigation, Formal analysis. **Hongjie An:** Investigation, Formal analysis. **Hong-Son Chu:** Methodology, Investigation. **Michael B. Sullivan:** Investigation. **Prince Nana Amaniampong:** Investigation.

Declaration of Competing Interest

The authors declare that they have no known competing financial interests or personal relationships that could have appeared to influence the work reported in this paper.

Data availability

Data will be made available on request.

Acknowledgements

This work was financially supported by the Australian Research Council (FL230100023 and DE240100408), the Vietnam National Foundation for Science and Technology Development (NAFOSTED) under grant number 104.05-2020.06 and by the Domestic Master/ PhD Scholarship Programme of Vingroup Innovation Foundation (the grant number VINIF.2019.ThS.79). T.L.V, H.K and P.T.H. would like to thank the RoHan Project funded by the German Academic Exchange Service (DAAD, No. 57315854) and the Federal Ministry for Economic Cooperation and Development (BMZ) inside the framework "SDG Bilateral Graduate school programme". M.B.S. and J.Z. would like to acknowledge the support from A*STAR's Accelerated Catalysis Development Platform (grant number A19E9a0103) and high-performance computational facilities from the National Supercomputing Centre (NSCC) Singapore (https://www.nscc.sg) and A*STAR Computational Resource Centre (A*CRC). Q.T.T. would like to acknowledge the National Computational Infrastructure (NCI) via the NCI Adapter Scheme Q4 2023 (project qp76) and the Griffith University Gowonda HPC Cluster for the use of computational resources.

Appendix A. Supporting information

Supplementary data associated with this article can be found in the online version at doi:10.1016/j.jallcom.2024.175322.

References

[1] D.S. Sholl, R.P. Lively, Seven chemical separations to change the world, Nature 532 (2016) 435–437.
[2] M.S. Mauter, I. Zucker, F. Perreault, J.R. Werber, J.-H. Kim, M. Elimelech, The role of nanotechnology in tackling global water challenges, Nat. Sustain. 1 (2018) 166–175.
[3] P. Myagmarsereejid, S. Suragtkhuu, Q.T. Trinh, T. Gould, N.T. Nguyen, M. Bat-Erdene, E. Campbell, M.T. Hoang, W.-H. Chiu, Q. Li, H. Wang, Y.L. Zhong, M. Batmunkh, Large-area phosphorene for stable carbon-based perovskite solar cells, npj 2D Mater. Appl. 8 (2024) 38.
[4] H. Xu, N. Liang, L. Cui, H. Zhang, B. Yang, Z. Jin, Synergistic effect of interface and defect engineering of MoC/MoO_2 nano dot encapsulated N-doped carbon nanoflowers for highly durable dye-sensitized solar cells, J. Colloid Interface Sci. 653 (2024) 1620–1629.
[5] L. Qin, M. Zhu, Y. Xia, X. Ma, D. Hong, Y. Tian, Z. Tie, Z. Jin, Multifunctional dual-anion compensation of amphoteric glycine hydrochloride enabled highly stable perovskite solar cells with prolonged carrier lifetime, Nano Res. 17 (2024) 5131–5137.
[6] C. Yan, X. Xue, W. Zhang, X. Li, J. Liu, S. Yang, Y. Hu, R. Chen, Y. Yan, G. Zhu, Z. Kang, D.J. Kang, J. Liu, Z. Jin, Well-designed Te/SnS_2/Ag artificial nanoleaves

for enabling and enhancing visible-light driven overall splitting of pure water, Nano Energy 39 (2017) 539–545.
[7] Y. Xiong, X. Liu, Y. Hu, D. Gu, M. Jiang, Z. Tie, Z. Jin, $Ag_{24}Au$ cluster decorated mesoporous Co_3O_4 for highly selective and efficient photothermal CO_2 hydrogenation, Nano Res. 15 (2022) 4965–4972.
[8] Y. Xiong, H. Chen, Y. Hu, S. Yang, X. Xue, L. He, X. Liu, J. Ma, Z. Jin, Photodriven catalytic hydrogenation of CO_2 to CH_4 with nearly 100% selectivity over Ag_{25} clusters, Nano Lett. 21 (2021) 8693–8700.
[9] W. Zhang, Z. Jin, Z. Chen, Rational-designed principles for electrochemical and photoelectrochemical upgrading of CO_2 to value-added chemicals, Adv. Sci. 9 (2022) 2105204.
[10] X. Jiang, J. Huang, Z. Bi, W. Ni, G. Gurzadyan, Y. Zhu, Z. Zhang, Plasmonic active "hot spots"-confined photocatalytic CO_2 reduction with high selectivity for CH_4 production, Adv. Mater. 34 (2022) 2109330.
[11] Z. Zhang, X. Jiang, B. Liu, L. Guo, N. Lu, L. Wang, J. Huang, K. Liu, B. Dong, IR-driven ultrafast transfer of plasmonic hot electrons in nonmetallic branched heterostructures for enhanced H_2 generation, Adv. Mater. 30 (2018) 1705221.
[12] S. Du, S. Lin, K. Ren, C. Li, F. Zhang, Revealing the effects of transition metal doping on CoSe cocatalyst for enhancing photocatalytic H_2 production, Appl. Catal. B: Environ. 328 (2023) 122503.
[13] M.A. Tekalgne, K.V. Nguyen, D.L.T. Nguyen, V.-H. Nguyen, T.P. Nguyen, D.-V. N. Vo, Q.T. Trinh, A. Hasani, H.H. Do, T.H. Lee, H.W. Jang, H.S. Le, Q.V. Le, S. Y. Kim, Hierarchical molybdenum disulfide on carbon nanotube–reduced graphene oxide composite paper as efficient catalysts for hydrogen evolution reaction, J. Alloy. Compd. 823 (2020) 153897.
[14] Y. Xiong, B. Li, Y. Gu, T. Yan, Z. Ni, S. Li, J.-L. Zuo, J. Ma, Z. Jin, Photocatalytic nitrogen fixation under an ambient atmosphere using a porous coordination polymer with bridging dinitrogen anions, Nat. Chem. 15 (2023) 286–293.
[15] T.T. Dang, T.L.A. Nguyen, K.B. Ansari, V.H. Nguyen, N.T. Binh, T.T.N. Phan, T. H. Pham, D.T.T. Hang, P.N. Amaniampong, E. Kwao-Boateng, Q.T. Trinh, Chapter 7 - Perovskite materials as photocatalysts: Current status and future perspectives, in: V.-H. Nguyen, D.-V.N. .Vo, S. Nanda (Eds.), Nanostructured Photocatalysts, Elsevier, 2021, pp. 169–216.
[16] B. Han, P. Zhu, Y. Liu, Q. Qiu, J. Li, T. Liang, T. Xie, Enhanced photocatalytic degradation activity via a stable perovskite-type $LaFeO_3/In_2S_3$ Z-scheme heterostructured photocatalyst: unobstructed photoexcited charge behavior of Z-scheme photocatalytic system exploration, J. Alloy. Compd. 901 (2022) 163628.
[17] X. Liu, T. Wang, G. Li, G. Liu, J. Qiu, Z. Guo, H. Hao, J. Dong, H. Liu, J. Xing, Cooperation or competition between piezocatalysis and photocatalysis of $Bi_4Ti_3O_{12}$ nanoflakes, J. Alloy. Compd. 936 (2023) 168367.
[18] S. Mehra, J. Saroha, E. Rani, V. Sharma, L. Goswami, G. Gupta, A.K. Srivastava, S. N. Sharma, Development of visible light-driven $SrTiO_3$ photocatalysts for the degradation of organic pollutants for waste-water treatment: contrasting behavior of MB & MO dyes, Opt. Mater. 136 (2023) 113344.
[19] M. Abd Elkodous, A.M. El-Khawaga, M.M. Abouelela, M.I.A. Abdel Maksoud, Cocatalyst loaded Al-$SrTiO_3$ cubes for Congo red dye photo-degradation under wide range of light, Sci. Rep. 13 (2023) 6331.
[20] C. Zhang, H. Qi, Y. Zhang, C. Li, Q. Zhang, G. Hu, Z. Li, Carbon/Mn_3O_4/$SrTiO_3$ microsphere photocatalyst for the efficient removal of high-concentration methylene blue from water, J. Chem. Technol. Biotechnol. 98 (2023) 1453–1464.
[21] S. Patial, V. Hasija, P. Raizada, P. Singh, A.A.P. Khan Singh, A.M. Asiri, Tunable photocatalytic activity of $SrTiO_3$ for water splitting: strategies and future scenario, J. Environ. Chem. Eng. 8 (2020) 103791.
[22] K. Aravinthkumar, E. Praveen, A. Jacquline Regina Mary, C. Raja Mohan, Investigation on $SrTiO_3$ nanoparticles as a photocatalyst for enhanced photocatalytic activity and photovoltaic applications, Inorg. Chem. Commun. 140 (2022) 109451.
[23] Y. Wu, Q. Chen, J. Liu, K. Fang, M. Zhang, T. Jing, Z. Li, G. Wang, Accurate fabrication and orientation of electron acceptor and donor active sites for enhancing photocatalytic overall water splitting, J. Mater. Chem. A (2024).
[24] M.O. Olagunju, X. Poole, P. Blackwelder, M.P. Thomas, B.S. Guiton, D. Shukla, J. L. Cohn, B. Surnar, S. Dhar, E.M. Zahran, L.G. Bachas, M.R. Knecht, Size-controlled $SrTiO_3$ nanoparticles photodecorated with Pd cocatalysts for photocatalytic organic dye degradation, ACS Appl. Nano Mater. 3 (2020) 4904–4912.
[25] M. Chen, S. Li, S. Zhong, X. Zhou, Y. Ge, J. Luo, X. Zhou, X. Zhou, Y. Zhong, Al-$SrTiO_3$ decorated with non-noble metal co-catalyst NC-W2N for boosting photocatalytic overall water splitting via enhancing interfacial redox activity and charge separation, J. Alloy. Compd. 947 (2023) 169515.
[26] B. Huang, Y. Liu, Q. Pang, X. Zhang, H. Wang, P.K. Shen, Boosting the photocatalytic activity of mesoporous $SrTiO_3$ for nitrogen fixation through multiple defects and strain engineering, J. Mater. Chem. A 8 (2020) 22251–22256.
[27] S.P. Mantry, N.K. Bharti, B. Modak, Enhancement of visible light-driven water splitting and CO_2 conversion activities of $SrTiO_3$ by tuning the dopant charge state, J. Phys. Chem. C. 128 (2024) 4383–4394.
[28] Z. Zhao, X. Zhang, Y. Lei, P. Yang, J. Fan, B. Zhang, S. Yin, Exceptional photocatalytic activity for Ag,Cr- $SrTiO_3$ activated by H_2O_2 for removal of organic pollutants, Mater. Res. Express 7 (2020) 015034.
[29] F.Y. Alzoubi, A.A. Ahmad, I.A. Aljarrah, A.B. Migdadi, Q.M. Al-Bataineh, Localize surface plasmon resonance of silver nanoparticles using Mie theory, J. Mater. Sci.: Mater. Electron. 34 (2023) 2128.
[30] M.M. Abouelela, G. Kawamura, A. Matsuda, A review on plasmonic nanoparticle-semiconductor photocatalysts for water splitting, J. Clean. Prod. 294 (2021) 126200.
[31] J. Zhao, S. Xue, R. Ji, B. Li, J. Li, Localized surface plasmon resonance for enhanced electrocatalysis, Chem. Soc. Rev. 50 (2021) 12070–12097.
[32] T.C. Ngo, Q.T. Trinh, N. Thi Thai An, N.N. Tri, N.T. Trung, D.H. Truong, B.T. Huy, M.T. Nguyen, D.Q. Dao, SERS spectra of the pesticide chlorpyrifos adsorbed on silver nanosurface: the Ag20 cluster model, J. Phys. Chem. C. 124 (2020) 21702–21716.
[33] T.W. van Deelen, C. Hernández Mejía, K.P. de Jong, Control of metal-support interactions in heterogeneous catalysts to enhance activity and selectivity, Nat. Catal. 2 (2019) 955–970.
[34] C. Sarkar, S.C. Shit, D.Q. Dao, J. Lee, N.H. Tran, R. Singuru, K. An, D.N. Nguyen, Q. V. Le, P.N. Amaniampong, A. Drif, F. Jerome, P.T. Huyen, T.T.N. Phan, D.-V.N. Vo, N. Thanh Binh, Q.T. Trinh, M.P. Sherburne, J. Mondal, An efficient hydrogenation catalytic model hosted in a stable hyper-crosslinked porous-organic-polymer: from fatty acid to bio-based alkane diesel synthesis, Green. Chem. 22 (2020) 2049–2068.
[35] G. Liu, Q.T. Trinh, H. Wang, S. Wu, J.M. Arce-Ramos, M.B. Sullivan, M. Kraft, J. W. Ager, J. Zhang, R. Xu, Selective and stable CO_2 electroreduction to CH_4 via electronic metal–support interaction upon decomposition/redeposition of MOF, Small 19 (2023) 2301379.
[36] P.N. Amaniampong, Q.T. Trinh, T. Bahry, J. Zhang, F. Jérôme, Ultrasonic-assisted oxidation of cellulose to oxalic acid over gold nanoparticles supported on iron-oxide, Green. Chem. 24 (2022) 4800–4811.
[37] G. Liu, P.R. Narangari, Q.T. Trinh, W. Tu, M. Kraft, H.H. Tan, C. Jagadish, T. S. Choksi, J.W. Ager, S. Karuturi, R. Xu, Manipulating intermediates at the Au–TiO_2 interface over InP nanopillar array for photoelectrochemical CO_2 reduction, ACS Catal. 11 (2021) 11416–11428.
[38] Q.T. Trinh, J. Yang, J.Y. Lee, M. Saeys, Computational and experimental study of the Volcano behavior of the oxygen reduction activity of PdM@PdPt/C (M=Pt, Ni, Co, Fe, and Cr) core–shell electrocatalysts, J. Catal. 291 (2012) 26–35.
[39] P.N. Amaniampong, Q.T. Trinh, K. De Oliveira Vigier, D.Q. Dao, N.H. Tran, Y. Wang, M.P. Sherburne, F. Jérôme, Synergistic Effect of High-Frequency Ultrasound with Cupric Oxide Catalyst Resulting in a Selectivity Switch in Glucose Oxidation under Argon, J. Am. Chem. Soc. 141 (2019) 14772–14779.
[40] Q.T. Trinh, A. Banerjee, Y. Yang, S.H. Mushrif, Sub-Surface Boron-Doped Copper for Methane Activation and Coupling: First-Principles Investigation of the Structure, Activity, and Selectivity of the Catalyst, J. Phys. Chem. C. 121 (2017) 1099–1112.
[41] Q.T. Trinh, A.V. Nguyen, D.C. Huynh, T.H. Pham, S.H. Mushrif, Mechanistic insights into the catalytic elimination of tar and the promotional effect of boron on it: first-principles study using toluene as a model compound, Catal. Sci. Technol. 6 (2016) 5871–5883.
[42] Q.T. Trinh, A. Banerjee, K.B. Ansari, D.Q. Dao, A. Drif, N.T. Binh, D.T. Tung, P.M. Q. Binh, P.N. Amaniampong, P.T. Huyen, M.T. Le, Upgrading of Bio-oil from Biomass Pyrolysis: Current Status and Future Development, in: S. Nanda, D.-V. N. Vo, P.K. Sarangi (Eds.), Biorefinery of Alternative Resources: Targeting Green Fuels and Platform Chemicals, Springer, Singapore, Singapore, 2020, pp. 317–353.
[43] L. Zhang, M.-W. Chang, Y.-Q. Su, I.A.W. Filot, E.J.M. Hensen, A theoretical study of CO oxidation and O_2 activation for transition metal overlayers on $SrTiO_3$ perovskite, J. Catal. 391 (2020) 229–240.
[44] M. Qureshi, A.T. Garcia-Esparza, G. Jeantelot, S. Ould-Chikh, A. Aguilar-Tapia, J.-L. Hazemann, J.-M. Basset, D. Loffreda, T. Le Bahers, K. Takanabe, Catalytic consequences of ultrafine Pt clusters supported on $SrTiO_3$ for photocatalytic overall water splitting, J. Catal. 376 (2019) 180–190.
[45] G. Kresse, J. Hafner, Ab initio molecular dynamics for liquid metals, Phys. Rev. B 47 (1993) 558–561.
[46] G. Kresse, J. Furthmüller, Efficiency of ab-initio total energy calculations for metals and semiconductors using a plane-wave basis set, Comput. Mater. Sci. 6 (1996) 15–50.
[47] Z.-J. Zhao, Z. Li, Y. Cui, H. Zhu, W.F. Schneider, W.N. Delgass, F. Ribeiro, J. Greeley, Importance of metal-oxide interfaces in heterogeneous catalysis: a combined DFT, microkinetic, and experimental study of water-gas shift on Au/MgO, J. Catal. 345 (2017) 157–169.
[48] Q.T. Trinh, K. Bhola, P.N. Amaniampong, F. Jérôme, S.H. Mushrif, Synergistic application of XPS and DFT to investigate metal oxide surface catalysis, J. Phys. Chem. C. 122 (2018) 22397–22406.
[49] S. Grimme, J. Antony, S. Ehrlich, H. Krieg, A consistent and accurate ab initio parametrization of density functional dispersion correction (DFT-D) for the 94 elements H-Pu, J. Chem. Phys. 132 (2010) 154104.
[50] W. Tang, E. Sanville, G. Henkelman, A grid-based Bader analysis algorithm without lattice bias, J. Phys.: Condens. Matter 21 (2009) 084204.
[51] G. Henkelman, A. Arnaldsson, H. Jónsson, A fast and robust algorithm for Bader decomposition of charge density, Comput. Mater. Sci. 36 (2006) 354–360.
[52] C. Ambrosch-Draxl, J.O. Sofo, Linear optical properties of solids within the full-potential linearized augmented planewave method, Comput. Phys. Commun. 175 (2006) 1–14.
[53] P. Blaha, K. Schwarz, F. Tran, R. Laskowski, G.K.H. Madsen, L.D. Marks, WIEN2k: an APW+lo program for calculating the properties of solids, J. Chem. Phys. 152 (2020).
[54] W. Du, T. Wang, H.-S. Chu, C.A. Nijhuis, Highly efficient on-chip direct electronic–plasmonic transducers, Nat. Photonics 11 (2017) 623–627.
[55] W. Du, T. Wang, H.-S. Chu, L. Wu, R. Liu, S. Sun, W.K. Phua, L. Wang, N. Tomczak, C.A. Nijhuis, On-chip molecular electronic plasmon sources based on self-assembled monolayer tunnel junctions, Nat. Photonics 10 (2016) 274–280.
[56] Z. Dong, M. Asbahi, J. Lin, D. Zhu, Y.M. Wang, K. Hippalgaonkar, H.-S. Chu, W. P. Goh, F. Wang, Z. Huang, J.K.W. Yang, Second-harmonic generation from Sub-5 nm gaps by directed self-assembly of nanoparticles onto template-stripped gold substrates, Nano Lett. 15 (2015) 5976–5981.

[57] S.H. Chu, D.J. Singh, J. Wang, E.-P. Li, K.P. Ong, High optical performance and practicality of active plasmonic devices based on rhombohedral $BiFeO_3$, Laser Photonics Rev. 6 (2012) 684–689.
[58] R. Li, Z. Liu, Q.T. Trinh, Z. Miao, S. Chen, K. Qian, R.J. Wong, S. Xi, Y. Yan, A. Borgna, S. Liang, T. Wei, Y. Dai, P. Wang, Y. Tang, X. Yan, T.S. Choksi, W. Liu, Strong Metal–support interaction for 2D materials: application in noble metal/TiB_2 heterointerfaces and their enhanced catalytic performance for formic acid dehydrogenation, Adv. Mater. 33 (2021) 2101536.
[59] D.C. Ford, A.U. Nilekar, Y. Xu, M. Mavrikakis, Partial and complete reduction of O_2 by hydrogen on transition metal surfaces, Surf. Sci. 604 (2010) 1565–1575.
[60] A. Staykov, S. Fukumori, K. Yoshizawa, K. Sato, T. Ishihara, J. Kilner, Interaction of SrO-terminated $SrTiO_3$ surface with oxygen, carbon dioxide, and water, J. Mater. Chem. A 6 (2018) 22662–22672.
[61] L. Amidani, A. Naldoni, M. Malvestuto, M. Marelli, P. Glatzel, V. DalSanto, F. Boscherini, Probing long-lived plasmonic-generated charges in TiO_2/Au by high-resolution X-ray absorption spectroscopy, Angew. Chem. Int. Ed. 54 (2015) 5413–5416.
[62] A.E. Becerra-Toledo, M.R. Castell, L.D. Marks, Water adsorption on $SrTiO_3$(001): I, Exp. Simula STM, Surf. Sci. 606 (2012) 762–765.
[63] W. Hou, S.B. Cronin, A review of surface plasmon resonance-enhanced photocatalysis, Adv. Funct. Mater. 23 (2013) 1612–1619.
[64] S. Linic, P. Christopher, D.B. Ingram, Plasmonic-metal nanostructures for efficient conversion of solar to chemical energy, Nat. Mater. 10 (2011) 911–921.
[65] W. Dong, X. Li, J. Yu, W. Guo, B. Li, L. Tan, C. Li, J. Shi, G. Wang, Porous $SrTiO_3$ spheres with enhanced photocatalytic performance, Mater. Lett. 67 (2012) 131–134.
[66] K. Jyoti, M. Baunthiyal, A. Singh, Characterization of silver nanoparticles synthesized using Urtica dioica Linn. leaves and their synergistic effects with antibiotics, J. Radiat. Res. Appl. Sci. 9 (2016) 217–227.
[67] J. Wang, Y. Wang, Y. Wang, X. Zhang, Y. Fan, Y. Liu, Z. Yi, Role of P in improving V-doped $SrTiO_3$ visible light photocatalytic activity for water splitting: a first–Principles study, Int. J. Hydrog. Energy 46 (2021) 20492–20502.
[68] T.T.N. Phan, A.N. Nikoloski, P.A. Bahri, D. Li, Optimizing photocatalytic performance of hydrothermally synthesized LaFeO3 by tuning material properties and operating conditions, J. Environ. Chem. Eng. 6 (2018) 1209–1218.
[69] Y. Wang, H. Tao, Y. Cui, S. Liu, M. He, B. Song, J. Jian, Z. Zhang, Investigations on tuning the band gaps of Al doped $SrTiO_3$, Chem. Phys. Lett. 757 (2020) 137879.
[70] Z. Wu, Y. Zhang, X. Wang, Z. Zou, Ag@$SrTiO_3$ nanocomposite for super photocatalytic degradation of organic dye and catalytic reduction of 4-nitrophenol, N. J. Chem. 41 (2017) 5678–5687.
[71] S. Ouyang, P. Li, H. Xu, H. Tong, L. Liu, J. Ye, Bifunctional-nanotemplate assisted synthesis of nanoporous $SrTiO_3$ photocatalysts toward efficient degradation of organic pollutant, ACS Appl. Mater. Interfaces 6 (2014) 22726–22732.
[72] G. Murugadoss, D.D. Kumar, M.R. Kumar, N. Venkatesh, P. Sakthivel, Silver decorated CeO_2 nanoparticles for rapid photocatalytic degradation of textile rose bengal dye, Sci. Rep. 11 (2021) 1080.
[73] Q.T. Trinh, K.F. Tan, A. Borgna, M. Saeys, Evaluating the structure of catalysts using core-level binding energies calculated from first principles, J. Phys. Chem. C. 117 (2013) 1684–1691.
[74] Q. Zhang, Y. Huang, L. Xu, J.-j Cao, W. Ho, S.C. Lee, Visible-light-active plasmonic Ag–$SrTiO_3$ nanocomposites for the degradation of NO in air with high selectivity, ACS Appl. Mater. Interfaces 8 (2016) 4165–4174.
[75] Z. Wu, Y. Xue, Z. Zou, X. Wang, F. Gao, Single-crystalline titanium dioxide hollow tetragonal nanocones with large exposed (101) facets for excellent photocatalysis, J. Colloid Interface Sci. 490 (2017) 420–429.
[76] P.N. Amaniampong, Q.T. Trinh, J.J. Varghese, R. Behling, S. Valange, S.H. Mushrif, F. Jérôme, Unraveling the mechanism of the oxidation of glycerol to dicarboxylic acids over a sonochemically synthesized copper oxide catalyst, Green. Chem. 20 (2018) 2730–2741.
[77] Z. Wu, C. Xu, Y. Wu, H. Yu, Y. Tao, H. Wan, F. Gao, ZnO nanorods/Ag nanoparticles heterostructures with tunable Ag contents: a facile solution-phase synthesis and applications in photocatalysis, CrystEngComm 15 (2013) 5994–6002.